Laser-induced Graphitization of Lignocellulosic Nanofiber and Lignin-based Substrate

Anna Fall

A thesis

submitted in partial fulfillment of the

requirements for the degree of

Master of Science

University of Washington

2025

Committee:

Anthony Dichiara

Renata Bura

Rick Gustafson

Program Authorized to Offer Degree:

School of Environment and Forest Sciences

University of Washington

Abstract

Laser-induced Graphitization of Lignocellulosic Nanofiber and Lignin-based Substrate

Anna Fall

Chair of the Supervisory Committee:

Anthony Dichiara

Department of Bioresource Science and Engineering

Laser-induced graphitization (LIG) has emerged as a promising technique for the synthesis of conductive carbon materials. This process involves the controlled ablation of a material using a laser beam, leaving behind a patterned conductive carbon material. This technology has garnered significant attention due to its potential applications in the fabrication of all-carbon electronics, including electronics, energy storage devices, and new technology. Current methods for laser-induced graphitization often rely on expensive pulsed lasers and petroleum-derived polymer substrates, limiting their scalability and sustainability. Additionally, recent research explores using renewable substrates, such as wood, cellulose paper, and other biomaterials for laser scribing, these approaches often necessitate the addition of harmful chemicals, such as fire retardants or metal catalysts, undermining their environmental and economic advantages.

To address these limitations, the present study investigated laser-induced graphitization of lignin-coated filter paper pre-adsorbed with cellulose nanofibrils using a low-cost, continuous diode laser with an output power of 10W. The Taguchi method, a statistical design of experiments technique, was employed to optimize the laser processing parameters and achieve tailored electrical conductivity and kerf roughness. As-synthesized materials were thoroughly characterized using four-point probe resistance measurements, optical microscopy, Raman spectroscopy, and X-ray diffraction to elucidate their structural and electrical properties. This work demonstrates a sustainable and cost-effective approach to laser-induced graphitization using lignocellulosic nanofiber and lignin-based substrate in combination with a continuous wave laser, offering a promising pathway for scalable fabrication of carbon-based electronics.

Contents

List of Figures

List of Tables

1 Introduction

1.1 Background

Carbon is the sixth most abundant element in the universe and one of the most chemically versatile [1, 2]. The two primary categories of carbon differ based on their atomic orientation: crystalline and non-crystalline [2]. Crystalline carbon materials encompass subcategories such as diamond, graphite, and graphene. This material is composed of stacked layers, each shaped in a hexagonal honeycomb, forming a three-dimensional crystal lattice [3]. The non-crystalline form of carbon, known as amorphous carbon, contains a mixture of sp^2 and sp^3-hybridized bonds, along with traces of heteroatoms in addition to carbon [1, 2, 4]. The types of conductive carbon mentioned above are made synthetically or synthesized from naturally occurring graphite. These techniques include chemical vapor deposition (CVD), exfoliation, pyrolysis, laser ablation, and more [5, 6, 7, 8]. Each technique has its own advantages and disadvantages such as cost, yield, and complexity.

The demand for conductive carbon surging and driven by its use in energy storage, electronics, and new technology [9]. The U.S. depends heavily on imported graphite due to the limited domestic mining of graphite, posing a supply chain risk for essential industries including energy storage production and electronic production. Furthermore, the need for this material will continue to increase with the growing reliance on technology [10]. To ensure a secure supply for the previously mentioned applications, domestic development to secure a stable supply of this critical material is imperative.

Previous studies have focused on two main components of laser-induced graphitization (LIG), the lasing substrate and the laser. These encompassing categories can be further subdivided into organic and synthetic substrates as well as continuous wave (CW) laser or pulsed

lasers. Organic substrates include but are not limited to wood, cork, and other bioresources. These organic materials are categorized as lignocellulosic materials meaning they contain lignin [11]. In addition to lignin, these organic materials are also composed of polysaccharides, namely cellulose and hemicellulose [12]. Cellulose and hemicellulose have a low tolerance for high heat and can be thermally degraded at low temperatures unless additional chemical treatments are applied. Contrarily, lignin is more thermally stable due to its composition primarily being aromatic rings making it a sufficient candidate for LIG without further treatment [13]. Due to the low thermal stability of cellulose and hemicellulose, it is common to add a chemical pretreatment to increase the thermal resistance or conduct LIG in an inert atmosphere (Ar, N_2, or H_2) to prevent combustion and maximize the degree of graphitization [11, 14]. Synthetic substrates include polyimide (PI), polyetheretherketone (PEEK), low-density polyethylene (LDPE), and other synthetic polymers [15, 16]. Though synthetic polymers are excellent LIG precursors due to their thermal stability, presence of aromatics, and scalability, they also have disadvantages [17]. These disadvantages include environmental concerns, limited options, mechanical limitations, and high cost [11]. In conjunction with the lasing substrate, the choice of laser is also important in LIG studies. Pulsed lasers offer notable advantages in LIG research over CW lasers, namely the size of the heat-affected zone is relatively small and reaches high temperatures for carbonization resulting in more control over the reaction. In contrast, CW lasers are limited by their precision and low peak power [18]. The disadvantages of pulsed lasers include high cost, maintenance complexity, and limited large-area processing. Contrarily, CW lasers may be chosen over pulsed lasers owing to low cost, high excitation energy and laser efficiency, and availability in table-top sizes [19].

LIG is an effective method for both direct patterning and rapidly reaching a moderately high degree of graphitization [14, 20]. Direct patterning on a substrate by a laser had many advantages including simplified fabrication steps, cost-effectiveness, design flexibility, and scalability [20, 21]. These materials can be applied to applications including a variety of sensors, energy storage devices, and electrodes [14]. Additionally, LIG can be conducted using a wide variety of carbonaceous precursors offering a multitude of options for conductive carbon synthesis without relying on graphite imports [22]. Noting the many advantages of LIG, there is promise for this technique to be scaled up to produce large quantities of conductive carbon for the previously mentioned applications that will continue to grow in popularity. This research aims to fill in the previously mentioned gap of LIG research by using untreated, organic substrate in combination with a cost-effective continuous wave laser.

1.2 Motivation

LIG studies use different combinations of the laser's defocus distance, power percent, speed, and number of passes to achieve conductive graphitic carbon. As mentioned, researchers can better regulate reaction temperature by using fire retardants or thermally tolerant substrates in conjunction with pulsed lasers and controlled atmospheres. This approach reduces the risk of substrate incineration and increases the probability of forming conductive graphitic carbon. As laser technology and materials science advance, there is a growing trend towards conducting LIG in ambient atmospheres to reduce cost and complexity. However, this often necessitates compromises. Utilizing ambient conditions involves the use of fire retardants impacting sustainability. Alternatively, implementing pulsed lasers offer greater control and precision, can increase costs. One of the common combination of recent research involves conducting LIG in ambient conditions using sustainable substrates and pulsed laser. While CW lasers are attractive

due to their low cost and simplicity, their high thermal energy and lower precision can cause problems including substrate incineration [19]. To eliminate these challenges, many CW laser LIG studies incorporate fire retardants or inert atmospheres, both of which increase cost and decrease sustainability and scalability. To further decrease costs while maintaining sustainability and scalability, this study demonstrates the feasibility of using a low-cost CW laser in conjunction with LIG in ambient conditions on lignocellulosic nanofiber and lignin-based substrate.

Electrical resistivity is a key performance parameter of conductive carbon. This parameter measures how resistance the graphitic carbon is to electrical current. Minimizing resistivity improves energy efficiency, signal integrity, and scalability of the conductive material being measured [23, 24]. All the mentioned material characteristics are important for the overall device performance. The method used to measure the resistivity of the graphitic carbon material is also important. This study uses the four-point probe method over the two-point probe method because the latter can introduce contact resistance, resulting in an inaccurate resistivity measurement [25].

Minimizing kerf roughness in electrically conductive carbon structures synthesized by laser-induced graphitization is also essential for realizing high-performance electronic devices. Inconsistent feature dimensions due to kerf roughness compromise device reliability and performance uniformity. In addition, rough features can introduce mechanical weaknesses, predisposing devices to failure under stress, thereby limiting their lifespan [26]. This is particularly relevant in flexible electronics where rough conductive traces are susceptible to cracking and failure during repeated bending. Similarly, in microfluidic devices incorporating laser-patterned electrodes, kerf roughness can disrupt uniform current distribution, negatively

affecting sensor accuracy and performance [27, 28]. Smoother kerfs are also crucial to achieve reliable interconnections and maintain signal integrity in printed circuit boards [29, 30].

1.3 Objective of present research

This research investigates LIG on lignocellulosic and lignin-based substrates. The primary objectives are to achieve optimal electrical conductivity, characterized by low resistivity, and ensure precise features, represented by low kerf roughness. Utilizing a completely organic substrate and cost-effective laser, the intent is to produce conductive graphitic carbon intended for diverse applications. Furthermore, this study seeks to demonstrate the precise control needed to fabricate consistent reliable features for devices.

2 Experimental methods

2.1 Materials and chemicals

Whatman ashless filter papers (70 mm diameter, 2.5 μm pore size) were purchased from GE Healthcare Life Sciences. Alkali lignin was obtained from Tokyo Chemical Industries through the sodium sulfite processing of softwood trees followed by subsequent desulfonation, oxidation, hydrolysis, and demethylation treatments. Swath-cut wheat straw was sourced from Co-op Supply (Marysville, WA). The following chemicals (ACS reagent grade or higher unless otherwise specified) were used for lignocellulosic nanofiber synthesis: peracetic acid (Sigma Aldrich), sodium hydroxide (VWR Chemicals BDH), hydrogen peroxide (Cascade Columbia Distribution), and diethylenetriamine pentaacetic acid (DTPA, 98+%; Acros Organics, Fisher Scientific). Deionized water was sourced from a Milli-Q plus water purification system (Millipore Corporate).

2.2 LCNF synthesis

Lignocellulose nanofibrils (LCNF) were synthesized following a previously reported method [31]. Briefly, non-cut wheat straw was initially pre-steamed and pre-soaked with deionized

water for 30 minutes before the addition of 7.5% (w/w) hydrogen peroxide (H_2O_2). The mixture was then cooked at 95 °C for 150 minutes. Following the alkaline pulping, the wheat straw pulp was then washed, mechanically treated, screened, and refined. Subsequently, a peracetic acid (PAA) reaction was performed in a rotary evaporator (25 rpm) for 50 minutes at 85 °C to then the reaction was quenched, and the fibers were washed followed by a 16-hour soak. Finally, the resulting PAA-treated fibers were blended for 30 minutes at 0.4 wt.% without further mechanical treatment producing LCNFs.

2.3 Substrate preparation

The LCNF and lignin-based substrate was prepared via vacuum-assisted filtration and drying. The Whatman papers were kept in a controlled room at 30% relative humidity and 20 °C for 24 hours. The moisture content was measured by weighing the wet Whatman paper, drying the Whatman paper for 24 hours, then weighing the dry paper. Equation (1) was used for calculating the moisture content,

$$Moisture\ content\ =\ \frac{wet\ mass - dry\ mass}{wet\ mass} \times\ 100 \quad (1)$$

Where the mass of the wet Whatman paper was weighed before the oven drying and the dry Whatman paper was weighed after oven drying.

Once moisture content was known, fresh Whatman papers were weighed on an Ohaus Pioneer scale. Thickness was taken using a Thwing Albert Thickness Tester and the TAPPI T411 caliper method. 0.4 wt.% LCNF suspended in DI water from LCNF synthesis was weighed prior to filtration with a target result of 15 wt.% LCNF layer on the Whatman paper. The pre-weighed Whatman filter paper was placed in the Büchner funnel and vacuum turned on. The pre-weighed LCNFs were poured over the filter paper and the water was removed via vacuum-assisted

filtration. After filtration, the wet LCNF-coated Whatman papers were weighed down with hollow weights and dried. The LCNF-coated Whatman papers dried for 24 hours in the controlled room, reweighed, and thickness measured using the same process as mentioned above. Moisture content was determined by the gravimetric method after drying in a conventional oven at 110 °C until the sample mass remained constant. 17 wt.% lignin solution was made by mixing DI water and softwood alkali lignin. The lignin coating was applied using a Fisher Scientific antistatic brush and the direction of the coating was kept the same for each replicate. The target weight percent of the lignin coating was 7 wt.%. Mass balance, moisture content, and thickness measurements were conducted after each step of the sample preparation process described above. Triplicate samples were prepared to ensure statistical soundness.

LIG of as-prepared substrates was conducted using the 450-nm emission of a continuous 10-W semi-conductor laser (Snapmaker 2.0, Shenzhen, China). The laser was operated at various focal distances (4-8 mm), laser power (26-30 %), scanning speed (2750-3250 mm/min), and number of passes (1-3). The laser patterned graphitic carbon both parallel and perpendicular to the brush strokes of the lignin coating. According to a study by Navarro-Segarra et al., the anisotropy of the graphitic carbon and placement of the four-point probe influences the resistivity [32]. Conductive graphitic carbon was obtained using various combinations of each of the above settings according to the L9 Taguchi array (Table 2.5.1).

2.4 Material characterization

The morphology of as-prepared cellulose samples was analyzed by scanning electron microscopy (SEM) before and after LIG using a ThermoFisher Scientific Apreo 1 operated at 5 kV. Non-irradiated samples were coated with a 4-nm layer of gold-palladium prior to SEM observations. The electrical conductivity of the different graphitic carbons was measured with a

Keithley 2450 source meter using a four-point probe configuration. Raman spectra of various graphitized samples were collected using a Renishaw InVia microscope equipped with a 785 nm laser excitation source. The I_D/I_G ratios were calculated using the Peak Pick function in Origin Pro. The A_D/A_G ratios were calculated using the area integration method in Origin Pro. XRD diffraction profiles were conducted at 50 kV on a Bruker D8 Discover using a high-efficiency Cu (1.54056 Å) anode and a 100 K Pilatus large-area 2D-detector. The crystallinity index of the pure cellulose, LCNF, lignin, and graphitic carbon layers was calculated using the area integration method in Origin Pro. Crystallite size L_a was calculated from XRD profiles using Equation 2, where λ represents the X-ray wavelength of 1.54 Å, θ is the Bragg angle of the peak, and $B_{1/2}(2\theta)$ is the full width at half maximum (FWHM) of the peak at angle 2θ fitted with Gaussian curve fitting.

$$L_a = \frac{1.84\lambda}{B_{1/2}(2\theta)\cos(\theta)} \qquad (2)$$

For comparison purposes, crystallite size, La, from the Raman spectra was calculated using Equation (3), where λ refers to the laser excitation wavelength (*i.e.* 785 nm), IG and ID are the intensity of the G- and D-bands extracted from the Lorentz fit of the Raman spectra, respectively.

$$L_a = (2.4 \times 10^{-10}) \times \lambda_l^4 \times \left(\frac{I_G}{I_D}\right) \qquad (3)$$

2.5 Design of experiment and statistics

Table 2.5.1 L9 Taguchi matrix with the mean, standard deviation, and signal-to-noise ratio (S/N) for the resistivity and kerf roughness responses.

Exp.	Defocus distance (mm)	Power (%)	Scan speed (mm/min)	#pass	Sheet resistivity (kΩ/□)	S/N ratio resistivity (dB)	Kerf roughness (μm)	S/N ratio kerf roughness (dB)
1	4	26	2705	1	1.12±0.52	-0.97	3.67±0.57	-10.58
2	4	28	3000	2	0.416±0.24	7.62	5.67±0.53	-15.07
3	4	30	3250	3	0.150±0.11	16.48	7.01±1.58	-16.91
4	6	26	3000	3	0.076±0.02	22.38	3.79±1.24	-10.73
5	6	28	3250	1	0.162±0.03	15.81	5.03±1.70	-14.03
6	6	30	2750	2	0.069±0.01	23.22	4.56±0.78	-13.18
7	8	26	3250	2	0.082±0.02	21.72	4.43±1.83	-12.93
8	8	28	2750	3	0.057±0.01	24.88	3.65±1.10	-11.25
9	8	30	3000	1	0.342±0.47	9.32	4.46±0.97	-12.99

The Taguchi method was applied to specify the optimum laser engraving conditions in the LIG process with the electrical resistivity and kerf roughness of the graphitized lignocellulose substrates being the independent objective functions. The laser defocus distance, defined as the distance between the laser beam's focal point and the substrate's surface, the scan speed, the laser power and the number of repeated engraving cycles were selected as control factors and their levels were determined based on preliminary experiments. The optimization study was conducted using a L9 orthogonal array (3^4) shown in Table 2.5.1, which describes the most efficient and structured

way to test the different combinations of factor levels with a minimal number of experiments. For each of the different combinations of factor levels, nine replicate electrical resistivity measurements were recorded on a Keithley 2450 SourceMeasure unit using the four-point collinear probe method. The kerf roughness of the various laser-graphitized structures was assessed by converting triplicate micrographs obtained from a Zeiss Axiolab optical microscope equipped with a 5 MP digital camera into binary images to calculate the mean kerf roughness from pixel counts and a scale bar using a Python script. Since the goal consists of minimizing both electrical resistivity and kerf roughness, the "smaller-is-better" function was employed to compute the Taguchi signal-to-noise (*S/N*) ratios, which quantify the effect of the control factors on the variability of the response, as shown in equation (4), where y_i refers to the observed data at the *ith* experiment and *n* is the number of observations of the experiment.

$$\frac{S}{N} = -10 \times \log\left(\frac{\Sigma(Y^2)}{n}\right) \qquad (4)$$

All experiments were designed and analyzed using Minitab Statistical Software version 22.1.0. The Taguchi method is a robust, powerful, and widely adopted engineering analysis method implemented that minimizes the number of experiments required to optimize system parameters [33].

3 Results and discussion

3.1 Material characterization

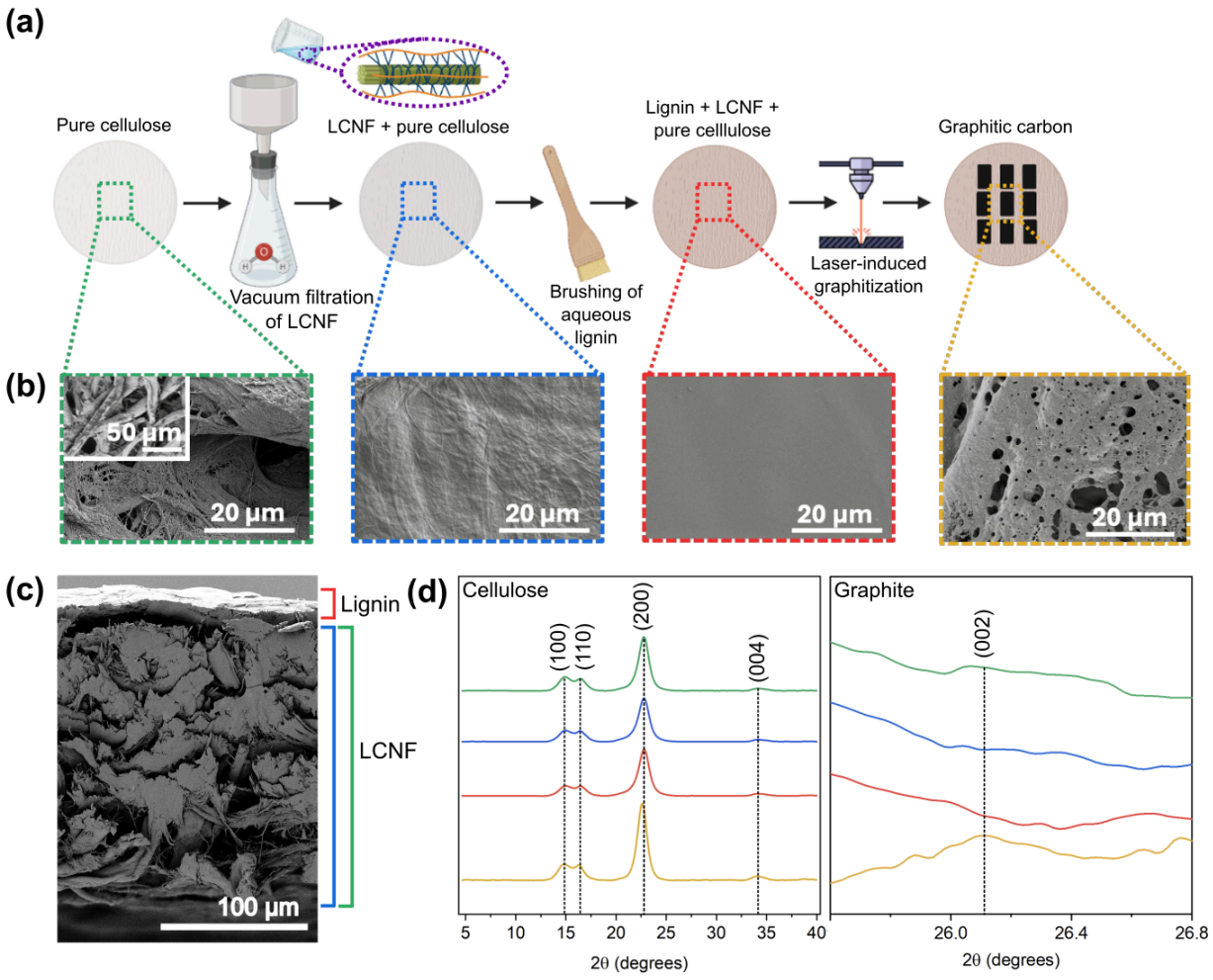

Figure 3.1.1 (a) Process flow diagram of substrate formation and graphitic carbon synthesis, (b) SEM images of pure cellulose paper layer, LCNF layer, lignin layer, and graphitic carbon, (c) cross section of layers substrate, (d) XRD spectra with Miller indices.

Prior to laser-induced graphitization (LIG), lignocellulosic substrates were fabricated as described in Figure 3.1.1a. Commercial ashless filter papers were initially embedded with LCNFs via vacuum infiltration. Subsequently, an aqueous lignin solution was applied uniformly onto the

LCNF-amended paper using a brush-coating method. SEM images, thickness, moisture content, and oven-dry mass were recorded after each sample processing step, as reported in Figure 3.1.1b and Table 3.1.1. SEM of the 190-μm thick pristine cellulose substrate reveals a porous structure characteristic of ashless filter papers comprising a combination of large (30.43 μm) and small (7.03 μm) pores. The LCNF infiltration effectively filled the material's pores, thereby displacing the oxygen within and inhibiting the substrate's incineration during laser exposure [34]. Due to their high aspect ratio, the loss of LCNF through the filtrate was less than 2% and the samples' LCNF content was 14.7 wt%. Following lignin coating, samples exhibited very uniform surfaces with a markedly smoother appearance, where brush strokes, LCNF, and individual cellulose fibers were no longer discernible. The lignin content after brush coating was 6.9±0.3 wt%. The substrate thickness measured using the TAPPI T441 caliper method was consistent with cross-sectional SEM observation and increased by 11% and 2% with the addition of LCNF and lignin, respectively (Table 3.1.1). SEM showed a flat, smooth surface with minimal porosity on the substrate, making it ideal for LIG. SEM analysis of the laser-irradiated samples indicated a three-dimensional network of interconnected pores, ranging from micro- to nanoscale, typical of carbon materials synthesized by laser graphitization of lignocellulose [35]. Representative XRD profiles of the samples after each processing step are depicted in Figure 1c and show the presence of diffraction peaks at 14.8°, 16.3°, and 22.6°, corresponding to the (100), (110), and (200) crystallographic phases of cellulose, respectively. The crystallinity index (Table 3.1.1) decreased from 96% to 87% and 85% after the addition of LCNF and lignin, confirming the successive incorporation of amorphous lignin in the substrate. Following LIG, the crystallinity index increased to 94%, suggesting the degradation of the amorphous components. In the XRD profile of the irradiated samples, the appearance of a small peak hidden by the intense cellulose reflections and centered

around 2θ=26.1°, reveals the formation of graphitic structures. This peak, which corresponds to (002) crystal phase of graphite is attributed to the interlayer spacing between graphene layers in graphitic carbon [35]. The slight tailing observed at smaller 2θ angles might be indicative of the presence of defects in the graphene layers.

Table 3.1.1 Physical properties of each layer.

Sample	Thickness (um)	Moisture (%)	OD-mass (mg)	Crystallite size (nm)	Lattice spacing (nm)	CI (%)
Pure cellulose	189.9±3.35	2.6±	372.5±7.37	45.9	0.39	96
After LCNF filtration	213.6±5.7	3.3±	428.1±7.93	42.8	0.39	87
After lignin brushing	218.2±6.3	3.2±	458.1±9.63	44.0	0.39	85
After LIG	-	-	-	51.1	0.39	94

3.2 LIG mechanism

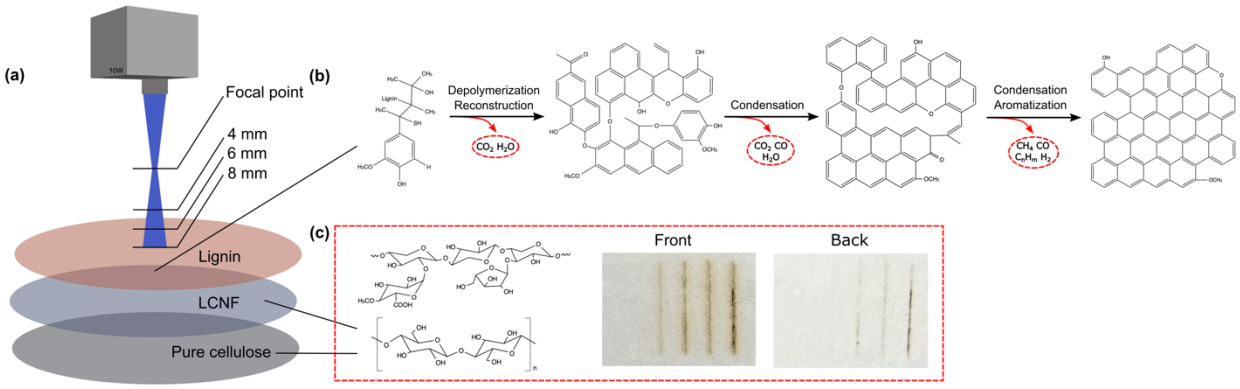

Figure 3.2.1 (a) Laser module with defocus distances and substrate layers, (b) lignin pyrolysis reaction, (c) experiment with only LCNF and pure cellulose substrate.

Figure 3.2.1a shows the focal point and defocus distances used in the L9 Taguchi array and each substrate layer and the graphitized region. Laser scribing on the pure cellulose and LCNF substrates revealed that without additional treatment or a pulsed laser, these materials alone were unsuitable precursors for LIG using the Snapmaker 10 W laser module (Figure 3.2.1c). On the front side of the scribed substrate, the first line segment exhibited no visual change. The subsequent two segments showed insufficient fluence for graphitization while the last segment displayed a burn-through indicating excessive fluence. On the back side, the last line segment displays complete burn-through. Moreover, the absence of black coloration in these lines indicated that no graphitization occurred (Figure 3.2.1c). Incorporating the lignin layer proved LIG successful. These findings suggests that the kinetics of lignin's thermal decomposition into graphitic carbon likely resembles that of the lignin pyrolysis processes. The primary reactions in lignin's thermal decomposition are free radical reactions (Figure 3.2.1b). During the lower temperature stages of laser ablation, lignin undergoes depolymerization, demethylation, side chain cleavage, and opening of aromatic rings. At higher temperatures, the thermal reaction concludes with deoxygenation and dehydration release gasses, and the subsequent closure of aromatic rings in a graphitic pattern [36].

3.3. Taguchi optimization of resistivity

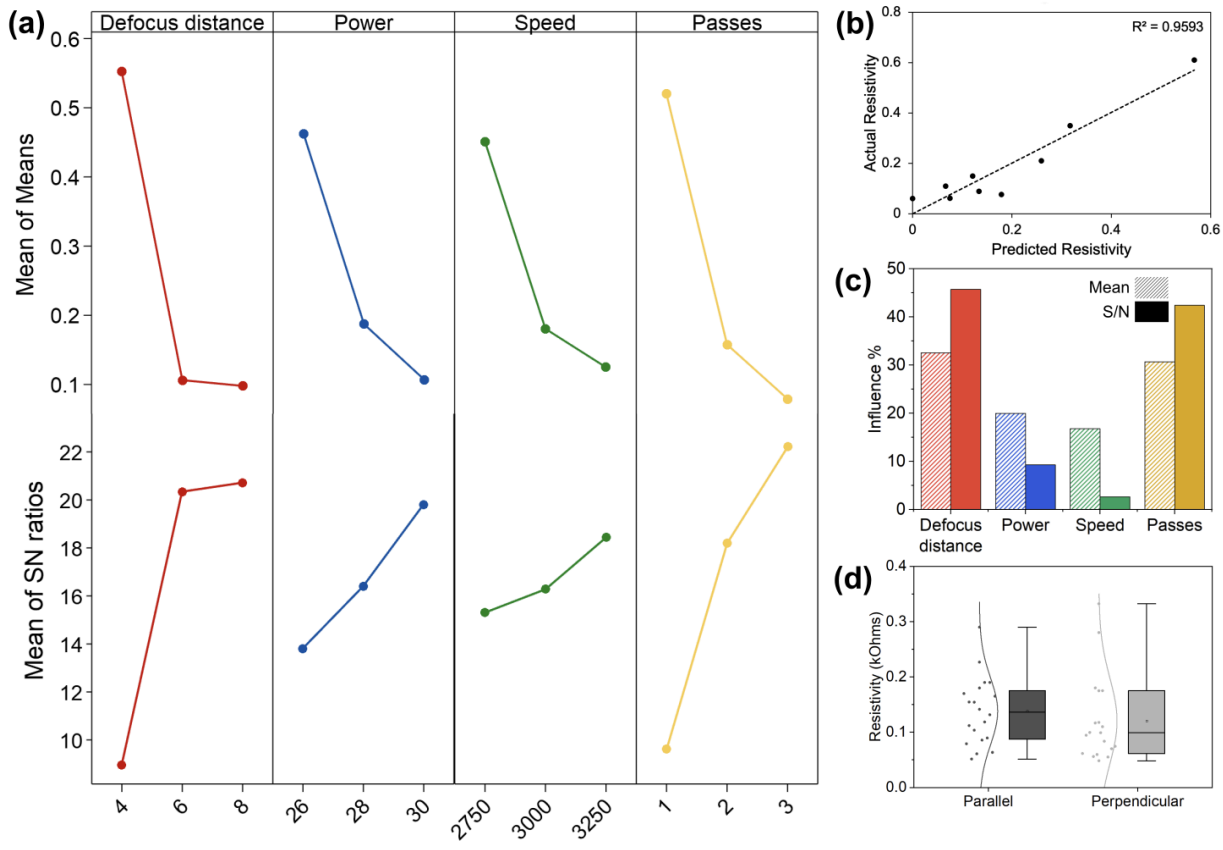

Figure 3.3.1 (a) Main effects plot of mean of means and mean of signal to noise ratio of perpendicular resistivity, (b) actual and predicted linear regression plot of perpendicular resistivity, (c) Pareto chart of factor influence on resistivity, based means and S/N ratios, (d) box plots of resistivity distribution for parallel and perpendicular anisotropy of graphitic carbon areas based on ANOVA.

A L9 Taguchi array (Table 2.5.1) was used to study the influence of various laser irradiation parameters on the properties of the resulting carbon materials with the electrical sheet resistance (Figure 3.3.1) and kerf roughness (Figure 3.5.1) being the objective function. In the case of four-point sheet resistance, triplicate rectangles with 9 by 13 mm^2 in size were engraved

for all the L9 orthogonal array experiments. Measurements were taken at three different locations on each engraved rectangle, for a total of 81 data points or nine replicates per orthogonal array experiment. Analysis of the main effects plot (Figure 3.3.1a) revealed that a combinations of 8 mm defocus distance, 30% power, 3250 mm/min speed, and 3 passes resulted in the lowest resistivity values. The "smaller-the-better" equation was used to calculate the S/N ratios for the resistivity, as lower resistivity corresponds to higher conductivity. An increased S/N ratio indicates a reduced variance of the resistivity, suggesting more uniform graphitic carbon. The proposed optimized parameters from the S/N plot (Figure 3.3.1) align with the main effects plot results, implying that these settings should achieve the least resistive and most uniform graphitic carbon. Linear regression analysis of resistivity in an R^2 value of 0.96, demonstrating good fit. The normal probability plot displayed the 9 resistivity averages close to the linear line, further supporting the linear regression model (Figure 3.3.1b).

An ANOVA analysis was conducted on the S/N ratios of resistivity for each factor of the Taguchi trial to identify the most influential laser parameter on graphitic carbon quality (Figure 3.3.1c). After conducting ANOVA at 95% confidence on the means and S/N ratios, the laser parameter with the greatest influence on quality is the defocus distance. As a result of ANOVA analysis, defocus distance and number of passes result in P-values less than the significance level of 0.05, indicating statistical significance. In contrast, power and speed exhibit P-values less than 0.05 suggesting that that have a negligible impact on the quality of the graphitic carbon. One-way ANOVA revealed no statistically significant difference between parallel and perpendicular anisotropy (Figure 3.3.1d). This is evident from the overlapping boxes in the box plot, which represents the middle 50% of the data. Therefore, further analysis will focus solely on perpendicular anisotropy. The optimized setting will now be referred to as the minimized

experiment given the minimization of resistivity and the non-optimized settings (4 mm defocus distance, 26% power, 2750 mm/min speed, and 1 pass) will now be referred to as the maximized experiment.

3.4 Validation of resistivity

After the L9 experiments, laser settings to minimize the resistivity were determined to be 8 mm defocus distance, 30% power, 3250 mm/min, and 3 passes. Contrarily, the laser parameters to maximize the resistivity were determined to be the same as experiment 1 in the L9 Taguchi table, therefore this experiment was not repeated. To validate the laser settings of the minimized trial, a confirmation trial was conducted with four replicates. This trial achieved a resistivity of 0.023 kΩ/□±0.001, demonstrating successful optimization. To further validate the results, ANOVA at 95% confidence was conducted on the minimized trial results. This analysis showed that the minimized resistivity is statistically significantly different from both the average resistivity and the lowest resistivity found in the original L9 trials. Moreover, the standard deviation of 0.001 is an order of magnitude smaller than the minimum standard deviation in the L9 table (Table 2.5.1). Additionally, the experimental S/N ratio of the resistivity was 27.23 which closely matches the 27.41 S/N ratio predicted from Minitab software.

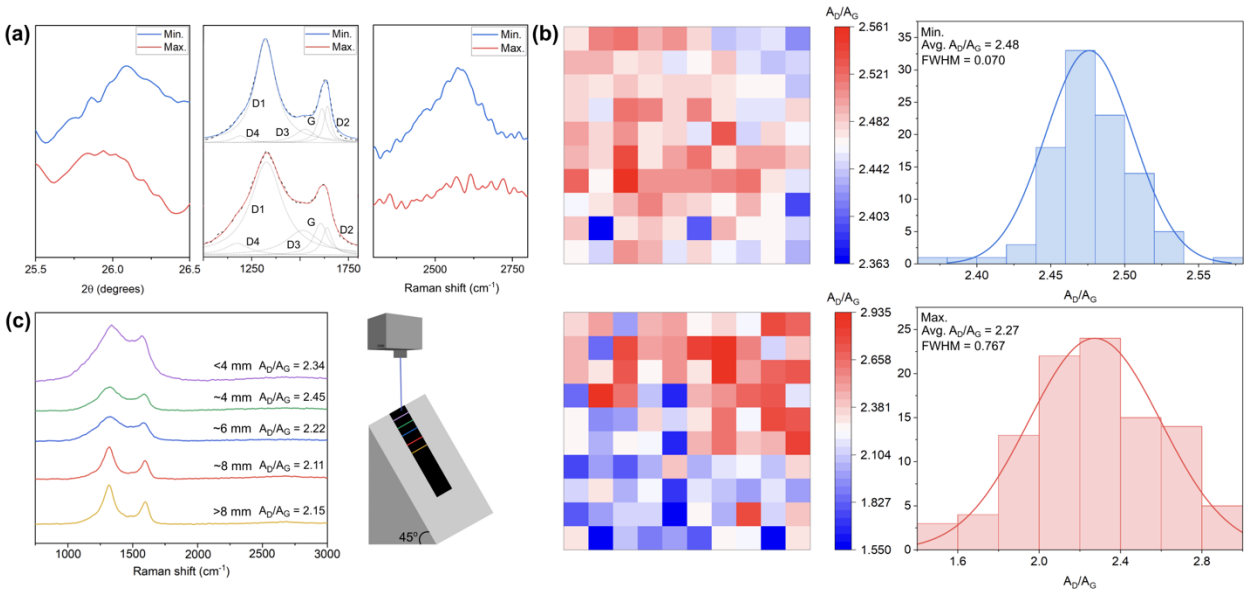

Figure 3.4.1 (a) XRD spectra (left), Raman spectra with deconvolution of minimum (top) and maximum (bottom) experiments, and 2D Raman spectra (right) of minimized (blue) and maximized (red) experiments, (b) 3 µm by 3 µm heatmap and distribution of optimized experiment, A_D/A_G ratios heatmap and distribution of minimized and maximized experiments, (c) smoothed Raman spectra of five spots on the angled graphitic carbon area.

Figure 3.4.1a shows XRD and Raman analysis of the minimized and maximized experiments in addition to an angled engraving trial. The (002) peak of the minimized experiment is sharper than that of the maximized experiment (Figure 3.4.1a). This is indicative of larger crystallite size and a more ordered graphitic carbon structure [37]. The minimized experiment exhibited a smaller interlayer spacing of 0.341 nm compared to the maximized experiment at 0.343 nm, suggesting more ordered graphitic carbon in the minimized sample [38]. Furthermore, the (002) peak shifts to higher 2θ values, indicating a decrease in the interlayer spacing. Notably, the L_a values for the minimized samples exceed those of the maximized samples, indicating the presence of larger in-plane graphitic domains, consistent with the sharp

peak in the XRD. This observation correlates with the reduced resistivity observed in the minimized samples, which can be attributed to enhanced electron mobility and reduced scattering at grain boundaries.

The five-peak model was employed to fit the first-order Raman data from 800 cm^{-} to 1800 cm^{-1}, with Lorentzian functions for D1, D2, D4, and G peaks and a Gaussian function for the D3 peak [39]. The goodness of fit was demonstrated by χ^2/dof below unity, with values of 0.3 and 0.04 for the minimized and maximized spectra, respectively. The G peak, located near 1580–1600 cm-1 is associated with sp2 bonded carbon atoms, while the D1 and D2 peaks centered around 1350 cm-1 and 1620 cm-1, respectively, are typically attributed to disordered sp^2 carbon, indicating the presence of defects both in the graphitic lattice and at the edges. The D3 and D4 peaks respectively located near 1500 cm-1 and 1200 cm-1 generally reveal the contribution of amorphous carbon. The ratio of band areas A_{D1} (arising from defective graphitic structures) and A_{D3} (arising from amorphous carbon), relative to A_G (arising from graphitic carbon), were used to compare the min and max samples. The A_G/A_{D1} and I_G/I_{D1} ratios in Table 3.4.1 indicate the proportion of graphitic to defective structures. The higher the A_G/A_{D1} or I_G/I_{D1} ratio, the fewer defects in the carbon structure. Given the maximized and minimized experiments have A_G/A_{D1} and I_G/I_{D1} ratios that are somewhat close means that each experiment has a similar density of defects in the carbon structures. Additionally, the A_G/A_{D3} and I_G/I_{D3} ratios indicate the degree of graphitic to amorphous carbon structures, the higher these ratios, the more graphitic structures are in the carbon. In Table 3.4.1, it can be seen that the minimized experiment has much higher A_G/A_{D3} and I_G/I_{D3} values than the minimized experiment, indicating more graphitic to amorphous structures than the maximized experiment [39].

Table 3.4.1 Minimized and maximized samples comparing Raman ratios and La values.

Structural Parameters	Minimized (opt)	Maximized (non-opt)
A_G/A_{D1}	0.147	0.151
A_G/A_{D3}	1.177	0.533
I_G/I_{D1}	0.334	0.342
I_G/I_{D3}	2.526	1.288
La (nm) XRD	48.107	31.838
La (nm) Raman	56.844	50.680

In addition, the lack of a distinct 2D peak in the second-order region near 2600 cm^{-1} further suggests that the maximized LIG conditions yielded a more amorphous and disordered carbon structure. The presence of a clear 2D peak in the minimized LIG samples confirms that the minimized experiment successfully converted the lignocellulosic nanofiber and lignin-based substrate into well-ordered graphitic structures with a higher degree of graphitization (Figure 3.4.1a). The comparison of crystallite sizes derived from Raman and XRD spectra are shown above (Table 3.4.1). The in-plane crystallite sizes (L_a) of the laser-induced graphitic structures, derived from both Raman spectroscopy and X-ray diffraction (XRD) analyses (Table 3.4.1) are in good agreement. These values are well aligned with previously reported published LIG studies [40].

Figure 3.4.1b displays heatmaps of the A_D/A_G ratios from mapping Raman scans of the minimized experiment and maximized experiment. The minimized sample's heatmap suggests the optimized laser settings produce a more consistent graphitic carbon structure across the whole sample. Additionally, the minimized experiment has a narrower FWHM in the Gaussian

distribution, implying a smaller range of A_D/A_G ratio variation. This is evident in the heatmap keys and the x-axis of the distribution plots. The minimized sample's A_D/A_G ratios range from 2.36 to 2.56 (a difference of 0.2), while the maximized experiment's range is 1.55 to 2.94 (a difference of 1.39). This offers advantages for applications by minimizing potential errors due to substrate inconsistencies. The heatmap of the maximized sample is more randomized and the FWHM of the Gaussian distribution is larger than that of the minimized sample. Although the maximized sample's A_D/A_G ratios are larger on average, it still exhibits greater uniformity. The higher A_D/A_G of the minimized sample compared to the maximized sample is most like due to the ambient atmosphere and the two additional passes of the optimized laser settings which generate more oxide species leading to more defects.

To assess the influence of defocus distance on the spot size and affects graphitization, a sample of lignocellulosic nanofiber and lignin-based substrate was set at a 45° angle then engraved using the minimized laser settings disregarding the defocus distance (Figure 3.4.1d). The laser beam reaches its focal point and maximum fluence at the top edge of the sample. As the laser moves down the sloped sample, the spot size increases, defocus distance increases, and fluence decreases. Spots 2 (green), 3 (blue), and 4 (red) approximately correspond to the defocus distances used in the Taguchi trial: 4mm, 6mm, and 8mm. The Raman peaks near 1300 cm^{-1} and 1590 cm^{-1} are indicative of D and G bands. The D and G bands of the optimized sample are more intense and sharper suggesting a higher concentration of graphitic carbon in the optimized sample. The D band is more intense than the G band on each spectra indicating the formation of a graphite-like structure. Analysis of the A_D/A_G values of each spot shows that the farther the defocus distance the better the graphitic carbon formation. This also corresponds to the resistivity where experiments with the defocus distance of 6 mm and 8 mm are generally less resistive than

the experiments with a defocus distance of 4 mm indicating that the resistivity and graphitic carbon formation are related.

3.5 Taguchi optimization of kerf roughness

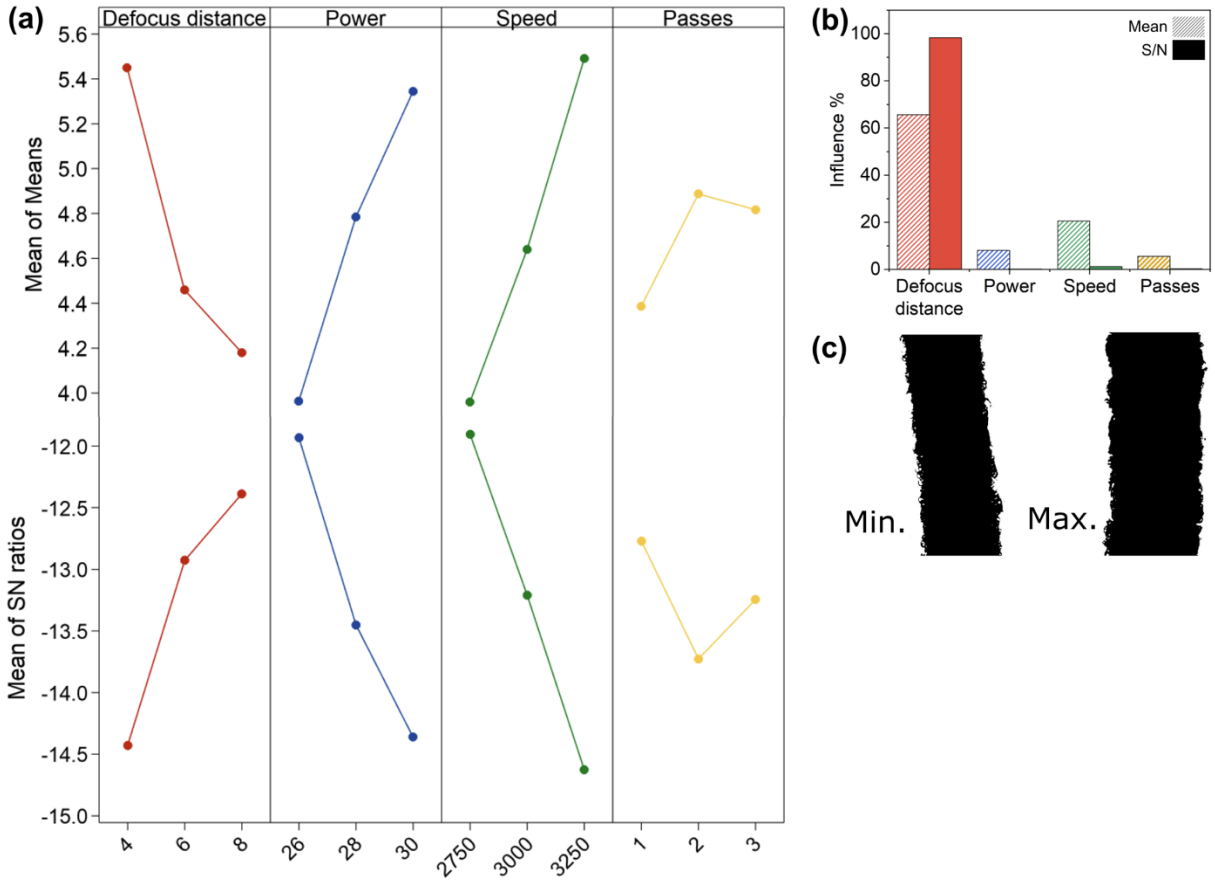

Figure 3.5.1 (a) Main effects plot of mean of means and mean of signal to noise ratio of kerf roughness, actual and predicted plot of kerf roughness, (b) Pareto chart of factor influence on kerf roughness, based means and S/N ratios, (c) kerf lines of minimized and maximized samples.

Similarly, kerf roughness optimization yielded an average of 3.44 um±0.27, demonstrating improvement. Additionally, the calculated S/N ratio of the kerf roughness was 220.01 while the predicted value was 10.87. For the kerf roughness optimization, duplicate lines

were engraved for all the L9 orthogonal array experiments, and triplicate measurements were taken from each line ensuring statistical soundness. The main effects plot (Figure 3.5.1a) shows that the optimized settings for kerf roughness differ from those for resistivity: 4 mm defocus distance, 28% power, 3000 mm/min speed, and 1 pass. The main effects plot and ANOVA analysis revealed that defocus distance is the most influential factor for kerf roughness, while the other laser parameters showed no significant effect. Following Taguchi analysis of resistivity and kerf roughness, Grey Relational Analysis was performed to optimize both response variables.

Grey Relational Analysis combines two or more responses into one response [41]. As the optimal settings for resistivity and kerf roughness differ, a multi-response Taguchi Grey Relational Analysis was conducted to determine optimized laser settings for both objectives. The analysis resulted in optimized laser settings of 8 mm defocus distance, 26% power, 2750 mm/min speed, and 1 pass. After running a validation trial to test the optimized laser settings determined by the Grey Relation Analysis, the resistivity was 0.37 kΩ/□±0.136 and the kerf roughness was 3.57 μm ±0.549. Each of these measurements fell within the L9 Taguchi experiments for resistivity and kerf roughness indicating a successful Grey Relation Analysis optimization.

3.6 Literature comparison

Table 3.6.1 Literature comparison containing substrate type, laser type, electrical characteristics, and the reference.

Substrate	Laser type	4-point resistivity (Ω/□)	Ref.
This work	450 nm continuous wave	23	-
Cellulose paper	10.6 µm CO_2 laser	61.5	[42]
Cellulose paper	10.6 µm CO_2 pulse laser	40	[43]
Cellulose paper	10.6 µm CO_2 continuous wave laser	32	[44]
Cellulose paper	10.6 µm CO_2 laser	51.3	[45]
Nanocellulose fiber	10.6 µm CO_2 laser	600	[46]
Nanocellulose fiber	10.6 µm CO_2 laser	2000	[47]
Nanocellulose fiber and kraft lignin	10.6 µm CO_2 laser	2000	[48]
Polyimide	10.6 µm CO_2 laser	15	[17]

Seen above in Table 3.6.1, the resistivity value of this research is lower than the resistivities of the other cellulose-based organic substrates. Additionally, polyimide is added at the end of the table to show how LIG of cellulose-based organic substrates compare to the most common synthetic substrate.

3.7 Practical application

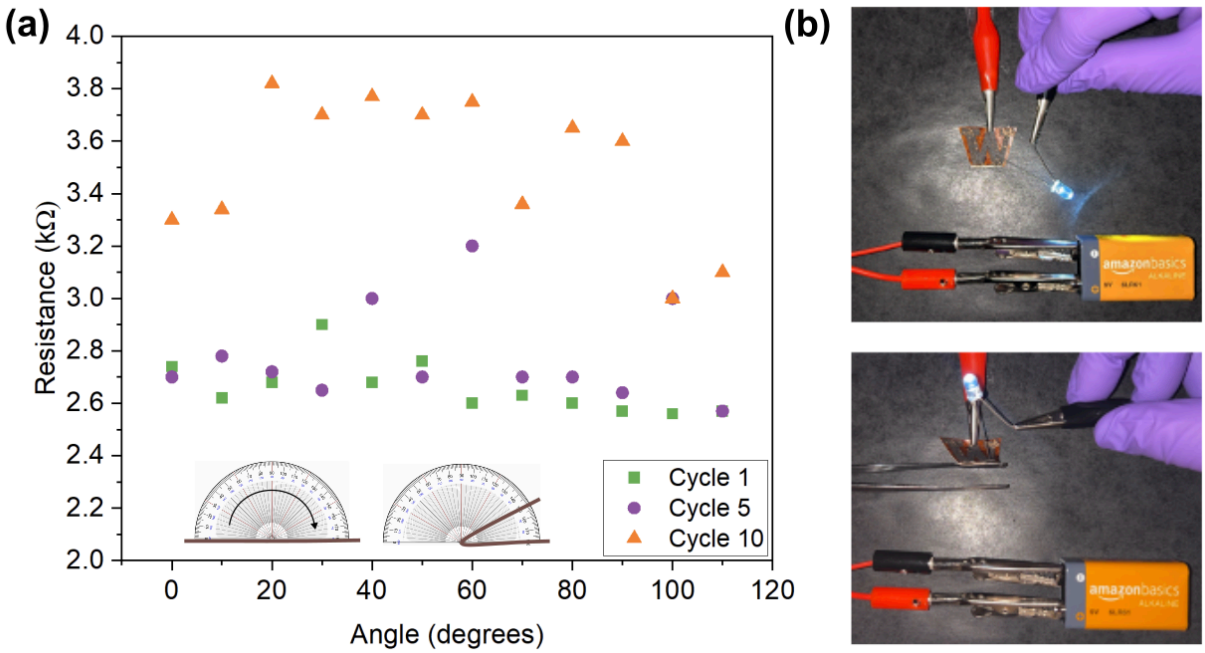

Figure 3.7.1 (a) Angle vs resistance graph for cycles 1, 5, and 10 with inlay of bending experiment diagram, (b) photos of minimized experiment plot flat and bent lighting up an LED with a 9V battery.

To demonstrate the application of this LIG substrate, an experiment testing the bending angle versus two-point resistance was conducted. The conductive carbon region measured for this experiment was prepared by using a strip of the LCNF and lignin-based substrate and conductive LIG using the optimized resistivity laser settings then engraving a 37 mm by 10 mm area of conductive carbon. Once the LIG was completed, copper tape was added to each end of the conductive carbon plot followed by silver paste to connect the copper tape to the conductive area. Once dry, the substrate was bent from 0° to 110° and the two-point probe resistance was recorded every 10° for 10 cycles. Figure 3.7.1 shows that the two-point resistance only slightly

varies when the angle is changed from 0° to 110° from 1 to 10 cycles. Figure 3.7.1b shows a graph of bending angle versus two-point resistivity at 1 cycle, 5 cycles, and 10 cycles. Overall, each plot has limited variability indicating that bending the sample does not interfere with the device performance. However, as the cycles increase, the resistance also increases due to the flakey composition of the graphitic carbon. The more times the sample is bend, the more the flakes are disrupted, and the contact area is decreased [49]. This demonstrates the ability of the LIG material can be used for flexible electronic devices without significantly changing the results. However, the more cycles, the slightly higher the resistivity due to the flakey structure of the graphitic carbon. This issue will be addressed in future studies.

4 Conclusion

Laser-induced graphitization can be done on lignocellulosic and lignin-based substrate without additional inorganic chemistry and with an economically accessible laser. Optimization of graphitic carbon resistivity and laser kerf using the Taguchi method has also proven successful. The resulting conductive carbon can be tuned by using the linear regression equation to calculate laser settings based on a target resistivity making this process a viable economically and environmentally sustainable substitute for graphitic carbon synthesis.

5 Acknowledgements

This thesis would not have been possible without the generous support from Weyerhaeuser, the United States Department of Agriculture, and the Department of Defense. I am also thankful to the Molecular Analysis Facility whose staff provided me with the equipment and training needed to complete my research. I am extremely thankful for the dependable support and encouragement of my advisor, Dr. Anthony Dichiara, whose unwavering belief in my capabilities motivated me, even in my most stressful and overwhelming moments.

To my parents who have raised me to have grit, determination, and fun with everything I do, I thank you. Thank you to my mom for showing me how to be a strong, successful woman in a competitive field. Thank you to my dad for teaching me how to bring creativity into everything I do and how to be compassionate to myself and others. Thank you to my stepdad for accepting me as one of your own and imparting your life lessons on me.

I am deeply thankful for my partner who is there for me during my highest of highs and lowest of lows. Jakob, your endless support in this rollercoaster of a journey has kept me strong and grounded. I must also express my appreciation for my friends who have always provided a fun distraction and stress relief in times when I needed it the most. Finally, I am beyond grateful for my three cats and leopard gecko, Bruce, Diego, Rango, and Petunia for unwavering love and comfort during this experience. This process has been an extremely rewarding experience and I have gone through extreme academic, professional, and personal growth from the beginning to the end.

6 References

[1] T. Gupta, Eds., *Carbon-The Black, the Gray and the Transparent*. Springer International Publishing, 2025.

[2] R. M. Hazem, A. P. Jones, & J. A. Baross, Eds., *Carbon in Earth*. Berlin: De Gruyter, 2013.

[3] J. Tucek, P. Blonski, J. Ugolotti, A. K. Swain, T. Enoki, & R. Zboril, "Emerging chemical strategies for imprinting magnetism in graphene and related 2D materials for spintronic and biomedical applications," *Chem Soc Rev*, vol. 47, no. 11, pp. 3899-3990, 2018. doi: 10.1039/C7CS00288B.

[4] H. Jager & W. Frohs, Eds., *Industrial Carbon and Graphite Materials: Raw Materials, Production and Applications*. Wiley, 2021.

[5] Y. M. Manawi, Ihsanullah, A. Samara, T. Al-Ansari, & M. A. Atieh, “A Review of Carbon Nanomaterials’ Synthesis via the Chemical Vapor Deposition (CVD) Method,” *Materials*, vol. 11, no. 5, pp. 822, 2018, doi: 10.3390/ma11050822.

[6] Y. Kwon, M. Liu, C. Castilho, Z. Saleeba, R. Hurt, & I. Kulaots, “Controlling pore structure and conductivity in graphene nanosheet films through partial thermal exfoliation,” *Carbon N Y.*, vol. 174, pp. 227-239, 2022, doi: 10.1016/j.carbon.2020.12.050.

[7] H. Kang, J. H. Oh, Y. H. Lee, S. Yang, & S. Choi, “Study on the Value-Added Carbon Products from Methane Pyrolysis with Thermal Plasma Process,” *Applied Science and Convergence Technology*, vol. 33, no. 1, pp. 13-17, 2024, doi: 10.5757/ASCT.2024.33.1.13.

[8] J. Tucek, P. Blonski, J. Ugolotti, A. K. Swain, T. Enoki, and R. Zboril, "Emerging chemical strategies for imprinting magnetism in graphene and related 2D materials for spintronic and biomedical applications," *Chem. Soc. Rev.*, vol. 47, no. 11, pp. 3899-3990, 2018. doi: 10.1039/C7CS00288B.

[9] Y. Zheng, X. Huang, J. Chen, K. Wu, J. Wang, and X. Zhang, "A Review of Conductive Carbon Materials for 3D Printing: Materials, Technologies, Properties, and Applications," *Materials*, vol. 14, no. 14, pp. 3911, 2021, doi: 10.3390/ma14143911.

[10] J. Zhang, C. Liang, & J. B. Dunn, “Graphite Flows in the U.S.: Insights into a Key Ingredients of Energy Transition,” Environmental Science & Technology, vol. 57, no. 8, pp. 3402-3414, 2023, doi: 10.1021/acs.est.2c08655.

[11] A. C. Bressi, A. Dallinger, Y. Steksova, & F. Greco, “Bioderived Laser-Induced Graphene for Sensors and Supercapacitors,” *ACS Applied Materials & Interfaces*, vol. 15, no. 30, pp. 35788-35814, 2023, doi: 10.1021/acsami.3c07687.

[12] R. Kaur, L. Pathak, & P. Vyas, “Biobased polymers of plant and microbial origin and their applications - a review,” *Biotechnology for Sustainable Materials*, vol. 1, no. 1, pp. 13, Oct. 2024, doi: 10.1186/s44316-024-00014-x.Laser-

[13] H. Yang, R. Yan, H. Chen, D. H. Lee, & C. Zheng, “Characteristics of hemicellulose, cellulose and lignin pyrolysis,” *Fuel*, vol. 86, no. 12, pp. 1781-1788, Aug. 2007, doi: 10.1016/j.fuel.2006.12.013.

[14] J. Edberg, R. Brooke, O. Hosseinaei, A. Fall, K. Wijeratne, & M. Sandberg, “Laser-induced graphitization of a forest-based ink for use in flexible and printed electronics,” *npj Flexible Electronics*, vol. 4, no. 17, 2020, doi: 10.1038/s41528-020-0080-2.

[15] A. Ghavipanjeh & S. Sadeghzadeh, “Simulation and experimental evaluation of laser-induced graphene on the cellulose and lignin substrates,” *Scientific Reports*, vol. 14, no. 4475, 2024, doi: 10.1038/s41598-024-54982-1.

[16] G. Liu & G. Xu, “Facile preparation of conductive carbon-based membranes on dielectric substrates,” *Front Chem.,* vol. 11, pp. 1152947, 2023, doi: 10.3389/fchem.2023.1152947

[17] J. Lin, Z. Peng, Y. Liu, F. Ruiz-Zepeda, R. Ye, E. L. G. Samuel, M. J. Yacaman, B. I. Yakobson, & J. M. Tour, “Laser-induced porous graphene films from commercial polymers,” *Nature Communication*, vol. 5, no. 5714, 2014, doi: 10.1038/ncomms6714.

[18] X. Jia, Y. Chen, L. Liu, C. Wang, “Combined pulse laser: reliable tool for high-quality, high-efficiency material processing,” *Opt. Laser Technol.,* vol. 153, pp. 108209, 2022, doi: 10.1016/j.optlastec.2022.108209.

[19] Z. Ismail, “Laser writing of graphene on cellulose paper and analogous material for green and sustainable electronic: a concise review,” *Carbon Letters*, vol. 32, no. 5, pp. 1227–1245, 2022, doi: 10.1007/s42823-022-00365-3.

[20] L. Cheng, C. S. Yeung, L. Huang, G. Ye, J. Yan, W. Li, C. Yiu, F. Chen, H. Shen, B. Z. Tang, Y. Ren, X. Yu, & R. Ye, “Flash healing of laser-induced graphene*,” Nature Communications*, vol. 15, no. 2925, 2024, doi: 10.1038/s41467-024-47341-1.

[21] Z. Wang, K. K. Tan, & Y. C. Lam, “Electrical Resistance Reduction Induced with CO_2 Laser Single Line Scan of Polyimide,” *Micromachines (Basel),* vol. 12, no. 3, pp. 227, 2021, doi: 10.3390/mi12030227.

[22] J.-F. Lataste, "Electrical resistivity for the evaluation of reinforced concrete structures," in *Non-Destructive Evaluation of Reinforced Concrete Structures,* vol. 2, Ed. Cambridge: Woodhead Publishing, 2010, pp. 243-275. doi: 10.1533/9781845699604.2.243.

[23] R. Ye, Y. Chyan, J. Zhang, Y. Li, X. Han, C. Kittrell, & J. M. Tour, “Laser-induced graphene formation on wood,” *Adv. Mater*., vol. 29, no. 37, 2017, doi: 10.1002/adma.201702211.

[24] S. Baek & J. S. Son, “Recent Advances in Direct Optical Patterning of Inorganic Materials and Devices,” *Advanced Physics Research*, vol. 3, no. 1, 2023, doi: 10.1002/apxr.202300069.

[25] R. D. Crapnell, E. Bernalte, R. A. A. Munoz, & C. E. Banks, “Electroanalytical overview: the use of laser-induced graphene sensors,” Anal. Methods, vol. 17, pp. 635-65, 2025, doi: 10.1039/D4AY01793E.

[26] A. Goyal & H. U. Rahman, “Experimental studies on Wire EDM for surface roughness and kerf width for shape memory alloy,” *Sādhanā*, vol 46, no. 160, 2021, doi: 10.1007/s12046-021-01684-3.

[27] T. S. Senthilkumar, R. Muralikannan, T. Ramkumar, & S. S. Kumar, “Studies of kerf width and surface roughness using the response surface methodology in AA 4032-TiC composites,” *Proceedings of the Institution of Mechanical Engineers*, vol. 235, no. 6, pp. 2240-2253, 2021, doi: 10.1177/09544089211041418.

[28] M. Płodzień, Ł. Żyłka, K. Żak, & S. Wojciechowski, “Modelling the Kerf Angle, Roughness and Waviness of the Surface of Inconel 718 in an Abrasive Water Jet Cutting Process,” *Materials (Basel),* vol. 16, no. 15, pp. 5288, 2023, doi: 10.3390/ma16155288.

[29] K. V. Rao, L. R. Raju, & C. K. Kumar, “Modeling of kerf with and surface roughness in wire cut electric discharge machining of Ti-6Al-4V,” *Proceedings of the Institution of Mechanical Engineers*, vol. 234, no. 6, pp. 533-542, 2020, doi: 10.1177/0954408920932369.

[30] M. Modi, G. Agarwal, S. Chaugaonkar, U. Bhatia, & V. Patil, “Effect of machine feed rate on kerf-width, material removal rate, and surface roughenss in machining of AL/SIC composite material, with wire electrical discharge machine,” *Journal of Mechanical Engineering*, vol. 20, no. 1, pp. 81-88, 2020, doi: 10.2478/scjme-2020-0008.

[31] D. U. Pascoli, A. Dichiara, R. Gustafson, & R. Bura, “A Robust Process to Produce Lignocellulosic Nanofibers from Corn Stover, Reed Canary Grass, and Industrial Hemp,” *Polymers*, vol. 15, no. 4, pp. 937, 2023, doi: 10.3390/polym15040937.

[32] M. Navarro-Segarra, O. A. Ibrahim, I. Martin-Fernandez, C. Tortosa, J. M. Ormaetxea, M. Baumann, M. Weil, & J. P. Esquivel, “Designed-by-purpose power sources: a cardboard primary battery for smart packaging,” *Royal Society of Chemistry*, vol. 24, pp. 5639-5652, 2024, doi: 10.1039/D4EE00306C.

[33] R. S. Rao, G. C. Kumar, R. S. Prakasham, & P. J. Hobbs, “The Taguchi methodology as a statistical tool for biotechnological applications: A critical appraisal,” *Biotechnology Journal*, vol. 3, no. 4, pp. 510-523, 2008, doi: 10.1002/biot.200700201.

[34] Z. Ismail, “Laser writing of graphene on cellulose paper and analogous material for green and sustainable electronic: a concise review,” *Carbon Letters*, vol. 32, no. 5, pp. 1227–1245, 2022, doi: 10.1007/s42823-022-00365-3.

[35] D. Deng, T. Li, Z. Huang, H. Jiang, S. Yang, & Y. Zhang, “Multi-response optimization of laser cladding for TiC particle reinforced Fe matrix composite based on Taguchi method and grey relational analysis,” *Opt. Laser Technol.*, vol. 153, pp. 108259, 2022, doi: 10.1016/j.optlastec.2022.108259.

[36] X. Lu & X. Gu, “A review on lignin pyrolysis: pyrolytic behavior, mechanism, and relevant upgrading for improving process efficiency,” *Biotechnology for Biofuels and Bioproducts*, vol. 15, no. 1, pp. 106, 2022, doi: 10.1186/s13068-022-02203-0.

[37] P. Bothi Raja, K. R. Munusamy, V. Perumal, and M. N. M. Ibrahim, "Characterization of nanomaterial used in nanobioremediation," in *Nano-Bioremediation: Fundamentals and Applications*, Eds. Oxford: Elsevier, 2022, pp. 57-83. doi: 10.1016/B978-0-12-823962-9.00005-X.

[38] J. Y. Hower, C. J. Rawn, L. E. Jones, & H. Ow, “Improved crystallographic data for graphite,” Powder Diffraction, vol. 18, no. 2, pp. 150-154, 2003, doi: 10.1154/1.1536926.

[39] Sadezky A, Muckenhuber H, Grothe H, Niessner R, o¨schl U. Raman microspectroscopy of soot and related carbonaceous materials: spectral analysis and structural information

[40] Zickler GA, Smarsly B, Gierlinger N, Peterlik H, Paris O (2006) A reconsideration of the relationship between the crystallite size of carbons determined by X-ray diffraction and Raman spectroscopy. Carbon 44:3239–3246

[41] P. A. Sylajakumari, R. Ramakrishnasamy, & G. Palaniappan, “Taguchi Grey Relational Analysis for Multi-Reponse Optimization of Wear in Co-Continuous Composite,” *Materials*, vol. 11, no. 9, pp. 1743, 2018, doi: 10.3390/ma11091743.

[42] H. Park, M. Kim, B. G. Kim, & Y. H. Kim, “Electronic functionality encoded laser-induced graphene for paper electronics,” *ACS Appl Nano Mater*, vol. 3, pp. 6899–6904, 2020, doi: 10.1021/acsanm.0c01255.

[43] Y. Chyan, J. Cohen, W. Wang, C. Zhang, & J. M. Tour, “Graphene art,” *ACS Appl Nano Mater*, vol. 2, pp. 3007–3011, 2019, doi: 10.1021/acsanm.9b00391.

[44] B. Kulyk, B. F. Silva, A. F. Carvalho, S. Silvestre, A. J. Fernandes, R. Martins, E. Fortunato, & F. M. Costa, “Laser-induced graphene from paper for mechanical sensing,” *ACS Appl Mater Interfaces*, vol. 13, pp. 10210–10221, 2021, doi: 10.1021/acsami.0c20270.

[45] X. Zang, C. Shen, Y. Chu, B. Li, M. Wei, J. Zhong, M. Sanghadasa, & L. Lin, “Laser-induced molybdenum carbide-graphene composites for 3D foldable paper electronics,” *Adv Mater*, vol. 30, no. 26, 2018, doi: 10.1002/adma.201800062.

[46] M. An, J. Wu, P. Wang, & Y. Fang, “Double-emission mechanism of laser-induced HOPG-exfoliated Graphene Quantum Dots (GQDs),” *Appl Phys Lett*, vol. 114, no. 2, 2019, doi: 10.1063/1.5081018.

[47] S. Lee & S. Jeon, “Laser-Induced Graphitization of Cellulose Nanofiber Substrates under Ambient Conditions,” *ACS Sustain. Chem. Eng*., vol. 7, no. 2, pp. 2270−2275, 2019

[48] F. Mahmood, Y. Sun, & C. Wan, “Biomass-Derived Porous Graphene for Electrochemical Sensing of Dopamine,” *RSC Adv*, vol. 11, no. 25, pp. 15410−15415, 2021, doi: 10.1039/D1RA00735A.

[49] I. S. Yoon, S. H. Kim, Y. Oh, B. K. Ju, & J. M. Hong, “Ag flake/silicon rubber composite with high stable and stretching speed insensitive resistance via conductive bridge formation,” Scientific Reports, vol. 10, no. 5036, 2020, doi: 10.1038/s41598-020-61752-2.